Nanoscale

ROYAL SOCIETY OF CHEMISTRY

MINIREVIEW

View Article Online
View Journal | View Issue



Cite this: *Nanoscale*, 2025, **17**, 2985

# NIR-II upconversion nanomaterials for biomedical applications

Ranran Luo,† Chenxi Zhang,† Zening Zhang,† Pengchen Ren, Zhongsheng Xu* and Yun Liu *

As a nonlinear optical phenomenon, upconversion (UC) occurs when two or more low-energy excitation photons are sequentially absorbed and emitted. Upconversion nanomaterials exhibit superior photostability, non-invasiveness, a unique near-infrared anti-Stokes shift, and enhanced tissue penetration capability. However, general upconversion nanomaterials typically utilize visible light (400–700 nm) for excitation, leading to limited tissue penetration, background signal interference, limited excitation efficiency and imaging quality issues due to tissue absorption and scattering. The increasing use of upconversion nanomaterials in the near-infrared one-region (NIR-I) window (700–900 nm) offers benefits such as enhanced penetration into biological tissues, relatively improved imaging resolution, and lower spontaneous luminescence, although these materials are still susceptible to background signals, limiting their effectiveness in high signal-to-noise ratio imaging. This distinctive wavelength conversion endows upconversion nanomaterials in the NIR-II region with extraordinary potential for diverse applications. Biomedical research has primarily focused on biomedical imaging for disease diagnosis and treatment, as well as biomarker detection. Nonetheless, studies specifically targeting the NIR-II window remain limited. This paper summarizes the latest research progress on upconversion nanomaterials in the NIR-II region. It begins by introducing the preparation methods for these materials in the NIR-II, followed by their applications in imaging and biological contexts. Lastly, it discusses the primary challenges and future prospects of upconversion materials in NIR-II, aiming to promote their development.

Received 27th October 2024,
Accepted 5th December 2024

DOI: 10.1039/d4nr04445b

rsc.li/nanoscale



## 1. Introduction

Upconversion materials exhibit a unique ability to produce anti-Stokes luminescence, known as upconversion luminescence (UCL), which converts low-energy photons into high-energy photons. This special wavelength conversion has broad-

*Department of Radiology, Second Affiliated Hospital of Chongqing Medical University, Chongqing 400010, China. E-mail: lrr990710@163.com, zhang_cx1206@126.com, 18833122821@163.com, 763111076@qq.com, zhongshengxu@cqmu.edu.cn, yunliu@cqmu.edu.cn*

† These authors contributed equally.

**Ranran Luo**

*Ranran Luo received her bachelor's degree in medical imaging from North Sichuan Medical College in 2021 and then continued to pursue her Master's degree at Chongqing Medical University. She majored in medical imaging and nuclear science under the supervision of Prof. Yun Liu. She is working on the design and preparation of nanosized formulations of natural medicines for the treatment of inflammation.*

**Chenxi Zhang**

*Chenxi Zhang received her bachelor's degree in medical imaging from Chongqing Medical University in 2023 and subsequently pursued her master's degree in medical imaging and nuclear science from the same university under the supervision of Prof. Yun Liu. Her research focuses on the design and synthesis of metal ion-based nano-formulations aimed at facilitating cancer therapy.*

ened the range of applications for upconversion materials in lasers, optoelectronic devices, displays, bio-detection, and bio-imaging.[1] The UCL mechanism was first proposed by Bloembergen and demonstrated by Porter in 1961. This process involves the absorption of energy by two or more low-energy photons, culminating in the emission of higher-energy photons. This phenomenon mainly occurs in the 4f orbital, where the shielding effects of the 5s and 5p shells on 4f electrons lead to intense emission and subsequent high photostability. The intrinsic forbidden nature of 4f–4f transitions promotes the sequential absorption of excitation states in individual lanthanide (Ln) ions and enables energy transfer between two or more Ln ions. Due to their unique f-electron configuration, rare-earth ions possess a multitude of energy levels and extended lifetimes, rendering them highly suitable for application as intermediate excited states in UCL.[2] Under appropriate excitation conditions, UCL can be produced by almost all rare-earth ions. $Er^{3+}$, $Ho^{3+}$, $Nd^{3+}$, and $Tm^{3+}$ are preferred activators owing to their energy levels, which facilitate the absorption of two or more photons of identical energy, thereby enabling UCL.[3,4] $Yb^{3+}$ is commonly employed as a sensitizer due to its straightforward energy level configuration and significant absorption cross-section, which facilitate the absorption of excitation photons and subsequent energy transfer to the activator. Yb/Er, Yb/Tm, or Yb/Ho co-doped materials can produce a variety of upconversion luminescence when co-doped with a suitable substrate and excited with a continuous laser.[5]

Upconversion materials emit light through anti-Stokes processes, contrasting with conventional down-conversion fluorophores (DCs) that follow Stokes' laws of optics, converting high-energy light into low-energy light. DCs offer advantages such as clear, adjustable emission peaks, high molar extinction coefficients and broad excitation spectra.[6] However, they suffer from drawbacks including significant autofluorescence background, limited tissue penetration despite high-energy laser excitation, photobleaching under diverse exposure conditions, phototoxic effects, broad emission spectra, and overlap between excitation and emission bands due to short Stokes shifts. To overcome challenges associated with conventional materials, researchers developed a novel fluorescent material leveraging atomic structural properties under low-energy light to induce higher-energy radiation. Categorized as an upconversion material following the anti-Stokes optical law, this material typically utilizes near-infrared radiation to stimulate emission in ultraviolet or visible light.[7]

Additionally, besides the aforementioned DCs, upconversion materials provide significant advantages compared to traditional light-emitting materials such as fluorescent dyes and semiconductor LEDs.[8] Firstly, they uniquely convert single-wavelength light into multiple wavelengths, including those in the visible range, enabling multi-wavelength and multimodal imaging. In contrast, the emission wavelength of dye materials is strictly determined by their molecular structure. Secondly, upconversion materials surpass dye materials in their resistance to light attenuation, maintaining stability and durability during prolonged irradiation thanks to specialized photophysical processes such as energy level structures and nonlinear optical properties. Thirdly, upconversion materials demonstrate high-resolution imaging and sensitivity, exhibiting higher luminescence efficiency and narrower bandwidths compared to common materials, which are more susceptible to environmental conditions. Additionally, they exhibit deep tissue transparency and multifunctional applications, expanding their utility across diverse scientific fields.[9,10]

Conventional visible light (360–830 nm) faces significant limitations: its shallow penetration depth (1–2 mm) and low signal-to-noise ratio. Thus, accessing diverse biological data in deeper tissue layers using visible light is challenging.[11] In addition, NIR-II upconversion nanomaterials offer better bio-

**Zening Zhang**

*Zening Zhang, currently a graduate student at Chongqing Medical University under the supervision of Prof. Yun Liu, is mainly engaged in the research of nanomaterials. Her research focuses on the application of nanomaterials in inflammation-related diseases, especially the application of nanocarriers in controlling drug delivery and immune regulation.*

**Yun Liu**

*Yun Liu is a professor in the department of radiology in the second affiliated hospital of Chongqing Medical University and a principle investigator in the molecular imaging and precision medicine laboratory. He received his bachelor's and doctoral degrees from Nanjing University of Science and Technology in 2011 and 2017, respectively. He also pursued his doctoral study in the department of chemistry at University of California, Riverside under the supervision of Prof. Yadong Yin from 2015 to 2017. His current research is focused on molecular imaging and nanomedicine.*

 

compatibility and safety than imaging techniques such as X-ray, CT and MRI. These nanomaterials are typically composed of non-toxic or low-toxicity chemical elements and can be gradually degraded in or excreted by the body, thus reducing the potential risk to living organisms. In contrast, X-ray and CT imaging may involve ionizing radiation, while MRI imaging requires the use of heavy metal contrast agents, which may cause some damage or discomfort to the organism. With advancements in optics, near-infrared one-region (NIR-I) has garnered increasing attention and thorough investigation. NIR-I offers reduced light absorption, scattering, and autofluorescence in tissues, enhancing radiation penetration. However, its clinical relevance remains limited.[12] In 2009, Welsher *et al.* achieved the first *in vivo* fluorescence imaging in the near-infrared (NIR) region beyond 1000 nm. This signaled the initiatory exploration of the near-infrared two-region (NIR-II, 1000–1700 nm).[13] NIR-II, compared to visible and NIR-I, significantly suppresses scattering effects and minimizes tissue autofluorescence. NIR-II offers a higher spatiotemporal resolution and more depth penetration (up to 30 mm) than NIR-I, making it more beneficial for clinical applications. Recent studies indicated that probes designed for NIR-II were more effective than those for NIR-I, despite most reports focusing on NIR-I probes. The growing interest and rapid expansion of the NIR-II region are driven by innovative research and groundbreaking advancements, highlighting its superior performance (Fig. 1).[14]

In summary, we introduce upconversion materials in the NIR-II and discuss the comparison between different preparation methods, as well as review a wide variety of biomedical applications of NIR-II upconversion materials.

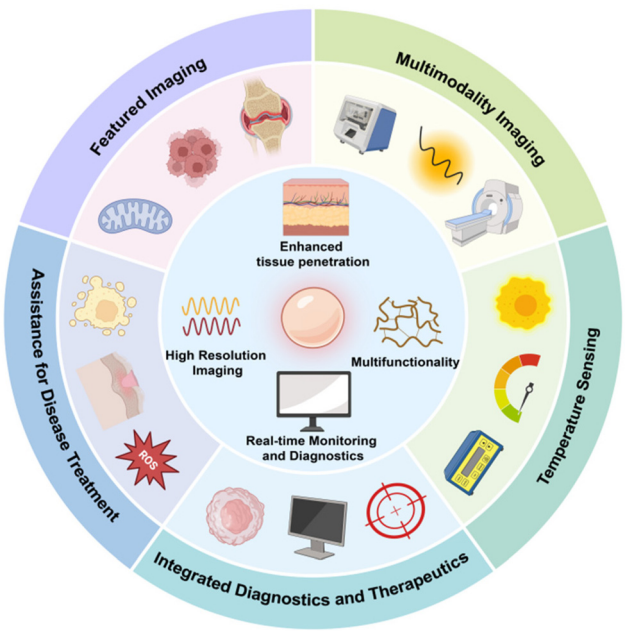


**Fig. 1** Schematic illustration of NIR-II upconversion nanomaterials for diverse applications.

## 2. Methods

### 2.1. Thermal decomposition

Thermal decomposition is renowned as one of the most effective techniques for synthesizing upconversion nanoparticles (UCNPs). In this procedure, metal–organic precursors are solubilized in a high-boiling-point organic solvent and subsequently decomposed at elevated temperatures to produce highly dispersed UCNPs. Frequently utilized metal–organic precursors include rare-earth organic compounds such as trifluoroacetate, acetate, and oleate. High-boiling-point organic solvents generally comprise mixtures of oleic acid (OA), octadecene (ODE), and occasionally oleylamine (OM). ODE is particularly selected to furnish a high-temperature environment for the reaction owing to its high boiling point (>300 °C).

The synthesis of highly monodisperse, monocrystalline, triangular nanoplates of $LaF_3$ with a thickness of 2.0 nm and an edge length of 16.0 nm *via* thermal decomposition of lanthanum trifluoroacetate ($La(CF_3COO)_3$) using a single-source precursor in an OA/ODE hot solution was first reported by Zhang *et al.*[15] In this process, ODE provides a high-temperature reaction environment, while OA acts as a coordinating surfactant due to its excellent coordination ability. Transmission electron microscopy (TEM) images revealed that $LaF_3$ nanocrystals (NCs) consisted of highly aligned arrays of triangular nanoplates, which were oriented either standing on the edge or lying flat on the surface, indicating a high degree of homogeneity in crystal size and preservation of oleic acid capping ligands. High-resolution electron microscopy (HRTEM) images showed vertically aligned triangular nanoplates flanked by six layers (002) with a face-to-face spacing of 0.36 nm and a thickness of 2.0 ± 0.1 nm. Additionally, the interparticle distance was approximately 2.4 nm, corresponding to the thickness of a single molecular membrane covering the oleate. This synthetic route established a new platform for the discovery of high-quality upconversion nanomaterials in the NIR-II region.

In 2018, Liu and colleagues reported $NaErF_4$:$Ln^{3+}$@$NaYF_4$ UCNPs ($Ln^{3+}$ = $Ho^{3+}$ or $Nd^{3+}$) with excitation and emission in the NIR-II region. Building on earlier studies, they produced β-$NaErF_4$:Ln core nanoparticles *via* the thermal decomposition of $Er(CH_3CO_2)_3{\cdot}4H_2O$ and $Ln(CH_3CO_2)_3{\cdot}4H_2O$ in an OA/ODE mixture. Subsequently, they prepared various core–shell nanoparticles using a one-pot, layer-by-layer (SLBL) method developed by their research group. By designing the core–shell structure and optimizing the doping concentration and the thickness of the shell layer, the NIR-II upconversion emission of $Er^{3+}$ (980 nm), $Ho^{3+}$ (1180 nm), and $Nd^{3+}$ (1060 nm) was achieved at 1530 nm (Fig. 2A).[16] In 2020, Huang *et al.* synthesized $NaErF_4$ core nanoparticles through a modified thermal decomposition method based on their previous studies. They then prepared core–shell nanoparticles by epitaxial growth on the core nanoparticles. They successfully realized inert shell-modulated multiplexed upconversion in UCNPs upon activation at 1530 nm (Fig. 2B).[17]

In a recent report, Feng *et al.* synthesized $LiYF_4$:10% $Er^{3+}$@$LiYF_4$, $NaYF_4$:10%$Er^{3+}$@$NaYF_4$ and $NaGdF_4$:10%

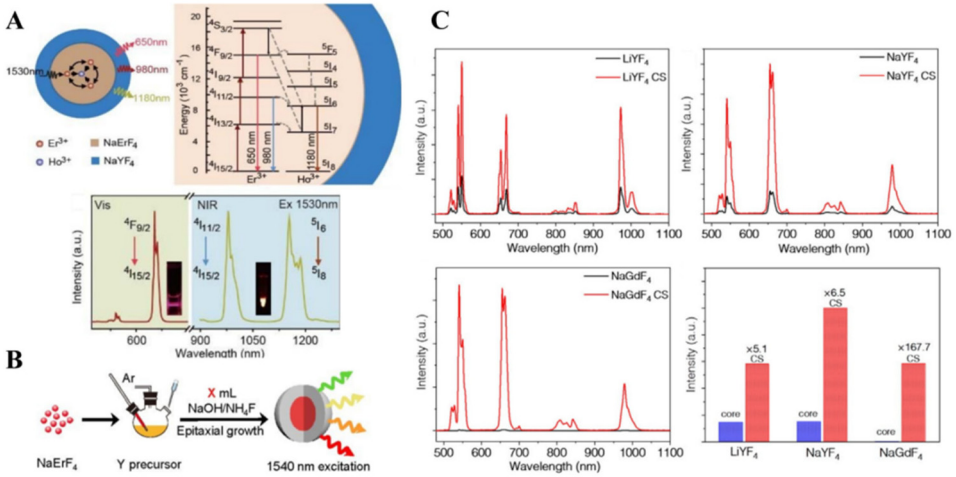


Fig. 2 (A) Energy transfer mechanism in the $NaErF_4$:2%Ho@$NaYF_4$ core/shell UCNPs and the upconversion emission spectrum of the obtained NIR-II UCNPs.[16] (B) Schematic illustration of the synthesis of the series of core–shell upconversion nanoparticles.[17] (C) UC emission spectra of core–shell nanoparticles, and the integration of their emission peaks excited at 1532 nm.[18]

$Er^{3+}$@$NaGdF_4$ core–shell nanoparticles using the thermal decomposition method.[18] The study corroborated that the concentration quenching effect was mitigated by the epitaxial growth of a homogeneous, inert protective layer. Consequently, the surface luminescence of the core–shell structures of $LiYF_4$, $NaYF_4$, and $NaGdF_4$ was enhanced by factors of 5.1, 6.5, and 167.7, respectively, under excitation at 1532 nm (Fig. 2C).

The results further confirmed the superior luminescence of UCNPs prepared *via* the thermal decomposition method in the NIR-II spectral range. However, the thermal decomposition method was air-sensitive, expensive, and toxic. Consequently, the co-precipitation method was developed as a viable alternative for synthesizing UCNPs.

From the above-mentioned literature, this method can precisely control the crystallization morphology of the material and is able to synthesize nanoparticles such as spherical, cubic, hexagonal prismatic, and other regular and highly crystalline nanoparticles. This regular morphology helps to realize the anisotropic optical properties of the materials, which is beneficial for the construction of high-performance optical devices as well as the effect of uniform dispersion and stable labeling in bio-imaging. Thermal decomposition allows fine tuning of the particle size, resulting in materials with smaller particle sizes (typically in the range of ten to several tens of nanometers) and narrower distributions. The small particle size enables good penetration in biomedical applications, which is suitable for deep tissue imaging and other scenarios with stringent requirements on particle size. Moreover, by optimizing the thermal decomposition conditions, such as choosing the appropriate temperature range and specific ligand assistance, the upconversion luminescence efficiency can be significantly improved, which can meet the requirements for high sensitivity biosensing, trace substance detection and other applications requiring high luminescence signal intensity. However, the reaction conditions are highly demanding, as even small variations in temperature and atmosphere can significantly impact luminescence efficiency. The process requires a controlled environment, with high equipment costs and operational complexity, which limits its applicability and scalability under standard conditions. Due to the complexity and high cost of synthesis, it is difficult to be used in large-scale industrial production of general civil optical products and is mostly used in scientific research and high-end biomedical diagnostics as well as other specialized fields with extremely high performance requirements.

### 2.2. Coprecipitation method

Coprecipitation is a more convenient method for preparing UCNPs, offering high yields, a simple synthesis process, and low cost. Typically, this method involves adding precipitants to a salt solution containing the cations of the desired material or directly hydrolyzing the salt solution at a specific temperature to produce ions in the precursor from various precipitates. Ultimately, better products can be achieved through the inherent processes of filtration, washing, drying, and roasting to decomposition.

The preparation of $NaYF_4$:$Ln^{3+}$ (Yb, Er) nanoparticles *via* co-precipitation of $Y^{3+}$, $Ln^{3+}$ with NaF in the presence of ethylenediaminetetraacetic acid (EDTA) was first reported by Yi *et al.*[19] They successfully obtained tunable nanoparticles with sizes ranging from 37 to 166 nm by adjusting the ratio of EDTA to $Ln^{3+}$. For instance, when $NaYF_4$:$Ln^{3+}$ nanoparticles were prepared using an EDTA/lanthanide molar ratio of 1 : 1, TEM images revealed spherical particles with an average diameter of approximately 40 nm and uniform size. However, these particles exhibited very weak upconversion fluorescence. The luminescence intensity significantly increased after 5 h of high-temperature treatment at 400–600 °C, leading to a phase transition from α (cubic) to β (hexagonal) in the UCP crystal

 

structure. The nanoparticles were highly dispersed in organic solvents, producing fluorescence emission from infrared to visible light. In 2017, Chen *et al.* presented a novel category of hexagonal-phase $NaErF_4$:Tm (0.5 mol%)@$NaYF_4$ nanocrystals with bright red upconversion luminescence *via* $Er^{3+}$-based sensitization.[20,21] They prepared $NaErF_4$:Tm core nanocrystals and then co-precipitated an inert shell layer of $NaYF_4$ as described in previous literature. Their research indicated substantial energy transfer among $Er^{3+}$ ions within erbium-dense $NaErF_4$:Tm@$NaYF_4$ core–shell nanoparticles, mitigating concentration quenching at the surface layer. Moreover, optimal doping of $Tm^{3+}$ further amplified the upconversion luminescence *via* energy trapping mechanisms.[22] This outcome produced nanoparticles exhibiting a significantly enhanced bright red coloration (an approximately 700-fold increase) and near-infrared luminescence, which can be achieved at various excitation wavelengths, specifically 808 nm, 980 nm, and 1532 nm (Fig. 3A). In 2018, Cheng *et al.* reported an innovative upconversion nanocrystal utilizing $Er^{3+}$ as a sensitizer. They synthesized controllable $NaYF_4$ (Fig. 3B) by a thermal co-precipitation method, serving as the host material. Under photo-excitation at 1532 nm, the excited $Er^{3+}$ ions were capable of transferring the absorbed energy to exciter ions, including $Nd^{3+}$, $Eu^{3+}$, $Ho^{3+}$, and $Tm^{3+}$. This energy transfer results in upconversion emission within the spectral range of 400–1200 nm, a process that is influenced by the co-doping of $Yb^{3+}$.[23] Moreover, $Er^{3+}$-sensitized photonic upconversion of $Ho^{3+}$ and $Tm^{3+}$ could be further enhanced by shell layers. Additionally, Peng *et al.* employed a modified co-precipitation technique, as adapted from previous research, to synthesize mono-doped $NaErF_4$:Tm@$NaYF_4$ core–shell nanoparticles and co-doped $NaYF_4$:Yb/Tm@$NaYF_4$ core–shell nanoparticles (Fig. 3C). Their study revealed that $Tm^{3+}$-doped UCNPs, when excited by near-infrared radiation at 1064 nm, 1150 nm, and 1208 nm, exhibited distinct upconversion behaviors.[24] Specifically, the 1150 nm excitation closely matched the energy gap between the $^3H_4$ and $^1G_4$ states, facilitating high-energy states that led to three- and four-photon blue emissions. In contrast, excitations at 1064 nm and 1208 nm predominantly resulted in two-photon emissions at 808 nm (Fig. 3D). Exploring the bursting effect of wavelength excitation in the NIR-II range, the study revealed that solvent burst, energy transfer, and cross-relaxation (CR) processes all have an influence on the upconversion emission of the $Tm^{3+}$-doped system (Fig. 3E).

The coprecipitation method has emerged as a popular and successful approach for preparing upconversion materials in the NIR-II region, and it has been widely applied in synthesizing various upconversion materials in this field.

According to the aforementioned literature, a variety of morphology materials can be synthesized by changing the conditions of precipitant type, concentration, reaction pH and temperature, such as spherical, rod, flake, dumbbell, *etc.*, which provide abundant choices for different application scenarios; for example, the rod material can be used to construct one-dimensional optical waveguide devices. Easy to operate,

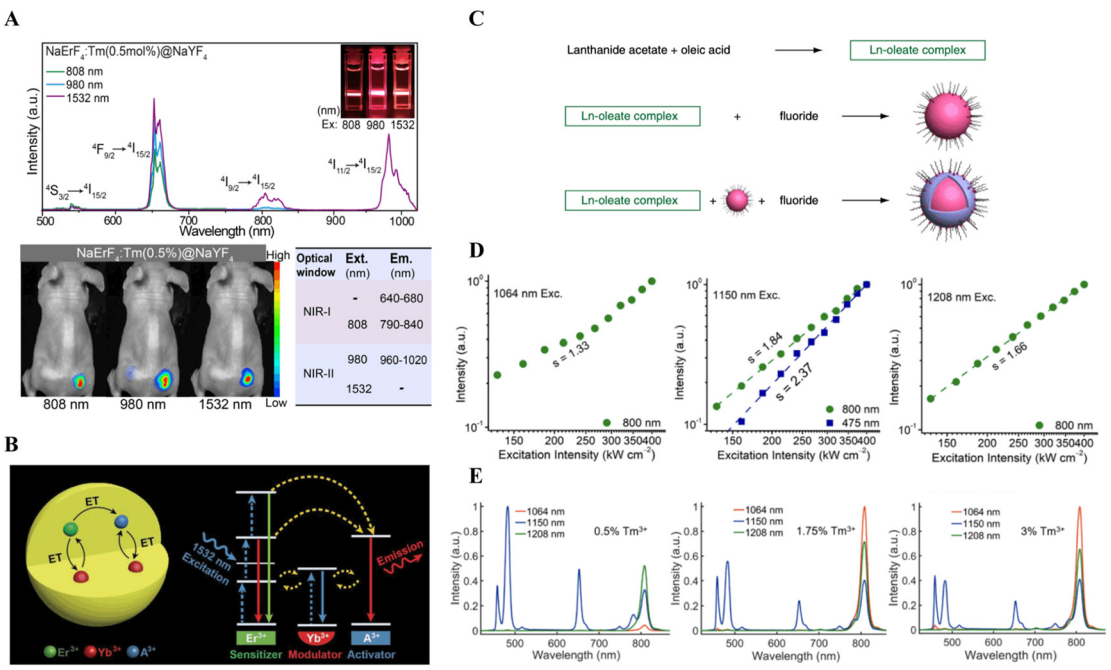


**Fig. 3** (A) Emission spectra, *in vivo* optical imaging and the compiled luminescence profiles for the as-synthesized nanocrystals when illuminated at 808, 980, and 1532 nm.[22] (B) Schematic illustration of $Er^{3+}$ sensitized photon upconversion under 1532 nm excitation.[23] (C) Schematic illustration of the co-precipitation strategy for the synthesis of lanthanide-doped $NaGdF_4$ and its core–shell nanocrystals. (D) Dependence of the emission intensities of the $NaYF_4$:Tm (1.75%) sample on excitation intensity at 1064 nm, 1150 nm, and 1208 nm, respectively. (E) Spectra of $NaYF_4$:Tm (0.5/1.75/3%) samples excited by NIR-II lasers at the intensity of 1.5 MW $cm^{-2}$.[24]

the materials with adjustable particle size from tens of nanometers to hundreds of nanometers can be rapidly synthesized at room temperature or lower temperature and atmospheric pressure, which is suitable for general application scenarios, such as simple cell labeling experiments, and is low-cost and easy to promote as described in the previous section. However, the homogeneity and regularity of the synthesized materials are poor, and they are prone to agglomeration, which affects the effective specific surface area and the consistency of the performance, and they perform poorly in high-end application scenarios (*e.g.*, high-resolution imaging) that require a precise morphology. In complex application environments requiring long-term stability and high optical performance (*e.g.*, long-time *in vivo* disease monitoring imaging, high-performance optical communication devices), the lack of stability of material performance and luminescence efficiency limits their applicability.

### 2.3. Solvent/hydrothermal synthesis

Hydrothermal synthesis has emerged as a simple and effective approach for producing high-quality upconverted nanomaterials, leveraging the high solubility and reactivity of feedstock reactants at elevated temperatures and pressures. In a conventional hydrothermal process, rare earth elements, typically in the form of rare earth chlorides, nitrates, and acetates, are utilized. Various fluorides such as HF, $NH_4F$, NaF, $NH_4HF_2$, $NaBF_4$, and HF are employed as fluoride precursors to synthesize $REF_3$ or $MREF_4$ (where M represents an alkali metal) compounds. The hydrothermal method, known for its convenience in synthesizing nanocrystals, involves adjusting various experimental parameters including the RE/F molar ratio, pH, fluoride precursor source, and the addition of $OH^-$ ions or ligand reagents like citric acid, EDTA, and cetyltrimethylammonium bromide (CTAB) to achieve the desired particle structure in the growth of nanoscale nanoparticles.

Wang and colleagues initially proposed a liquid–solid–solution (LSS) method for synthesizing diverse nanocrystals through phase transfer and separation. This approach involved three distinct phases: a liquid phase comprising linoleic acid and ethanol, a solid phase consisting of sodium linoleate, and a process that includes noble metals and product separation to eventually produce nanoparticles. The resulting LSS-synthesized nanoparticles (NPs) are dispersible or solubilized in nonpolar solvents like cyclohexane due to the hydrophobic alkyl chains covering their surface, which further prevents agglomeration. Varying the synthesis conditions, such as doping concentration, reaction temperature, and time, using the LSS strategy can produce different shapes of UCNPs.[25] In 2021, Zhang *et al.* designed a near-infrared II (NIR-II) phototherapy system for biomedical applications involving titanium.[26] The system was composed of upconversion element-doped titanium dioxide nanorods ($TiO_2$ NRs), curcumin (Cur), hyaluronic acid (HA), and bone morphogenetic protein-2 (BMP-2) (Fig. 4A). They synthesized $TiO_2$ using a hydrothermal method and then grafted Cur and BMP-2 onto the surface of the NRs *via* electrostatic adsorption binding. Co-doping of F, Yb, and Ho into the $TiO_2$ NRs not only conferred the upconversion ability, but also enhanced the photocatalytic performance

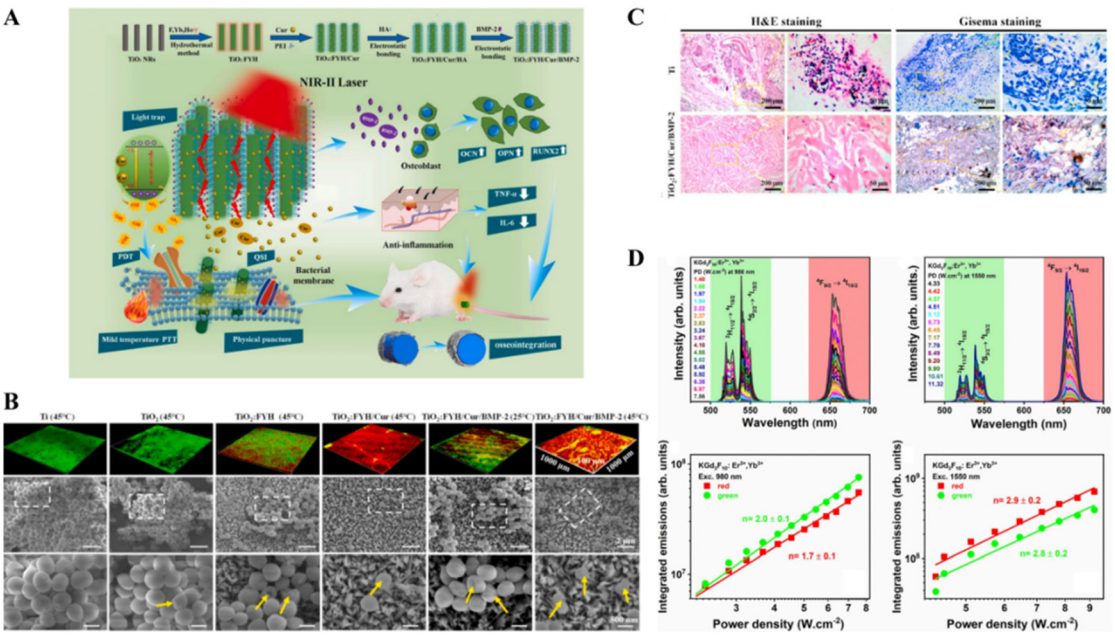


**Fig. 4** (A) Schematic illustration of the crafting process of the $TiO_2$:FYH/Cur/BMP-2 NRs on Ti implant towards biofilm elimination, anti-inflammation, and bone regeneration. (B) Fluorescence images and SEM images of the physiological changes of *S. aureus* irradiation with a 1060 nm laser for 15 min. (C) Images of H&E and Giemsa staining of soft tissue around Ti and $TiO_2$:FYH/Cur/BMP-2 implants. Neutrophils and bacteria are indicated by red and yellow arrows, respectively.[26] (D) UC emission spectra and the respective log–log plot of the areas under the UC spectra of the green and red emission bands as a function of the 980 and 1550 nm excitation power densities, respectively.[27]

 

of $TiO_2$. The hybrid NRs exhibited outstanding anti-biofilm properties *in vitro* (Fig. 4B) and *in vivo* (Fig. 4C) under 1060 nm light at a relatively low temperature (45 °C). In a recent publication, Karmel de Oliveira Lima and colleagues synthesized $KGd_3F_{10}$ NPs doped with 5% $Er^{3+}$ and 20% $Yb^{3+}$ using an ethylenediaminetetraacetic acid-assisted hydrothermal method (Fig. 4D).[27]

The solvent/hydrothermal method presents several advantages for the synthesis of high-quality UCNPs. These advantages include the ease of controlling the size, structure, and shape of the nanoparticles, achieving high purity, employing a simple process, and utilizing cost-effective and time-efficient equipment.

This method is known to have a strong ability to regulate the morphology; by changing the type of solvent, filling degree, reaction temperature and time, and other factors, nanoflowers, nanorod bundles, hollow nanostructures and other complex fine-structured materials can be synthesized. These special morphologies can endow the material with unique optical, electrical and other properties, such as a hollow structure for light scattering and adsorption properties for photocatalysts, bio-imaging and other applications. The ability to synthesize nanomaterials with uniform and relatively small particle sizes (tens to hundreds of nanometers), and the consistency of particle sizes in large-scale synthesis, facilitates the mass production of materials and the maintenance of stable performance in practical applications, such as the mass production of diagnostic reagents for bio-imaging. However, the reaction is carried out in a closed reactor, which makes it difficult to monitor it in real time and adjust the morphology flexibly in the middle of the process. Very high accuracy of the reaction conditions is also required, and a small deviation may lead to a material morphology that is not in line with the expectations and difficult to correct, which restricts the controllable preparation of materials with a precise morphology. It is difficult to precisely control the particle size to a very small range (a few nanometers), which makes it difficult to meet the needs of cutting-edge nano-optics research on ultra-fine particle size materials, such as the construction of quantum dot-level optical devices. Moreover, the post-processing of the reacted materials can easily destroy the crystalline structure and affect the luminescence efficiency and stability if the operation is not done properly, so the subsequent processing needs to be strictly controlled, which increases the difficulty and cost of preparing high-quality materials. In addition to the four synthesis methods mentioned above, we can also refer to other methods such as the common self-assembly and sol–gel methods. The self-assembly method also plays an important role in the construction of upconversion materials, which involves the pre-preparation of various monomer components, which are then combined in a nanosystem to form the desired nanoparticles.[28,29] A number of papers have demonstrated that self-assembly enables the convenient combination of upconverted nanoparticles with different types of functional materials to construct nanocomposites that combine multiple functions.[30–34] For example, on the one hand, upconversion nanoparticles can be used to realize deep tissue imaging by using near-infrared light-excited luminescence; on the other hand, they can be combined with drug molecules to achieve targeted drug release, or with photothermal/photodynamic therapeutic reagents to achieve integrated diagnosis and treatment to satisfy the current growing demand for multifunctional nanomaterials in the field of biomedicine and other fields.[30] Because the self-assembly process is mostly carried out under relatively mild conditions such as room temperature and pressure, unlike some traditional synthesis methods (*e.g.*, high-temperature thermal decomposition, *etc.*) that require extreme reaction environments, this not only reduces the requirements for equipment and energy, but also, more importantly, helps to maintain the biocompatibility of the upconverted nanoparticles themselves as well as the assembled system. In biomedical application scenarios, this good biocompatibility allows the materials to better interact with the internal environment of the organism and reduces adverse effects such as immune reactions, which is conducive to the promotion of their applications in cell labeling, *in vivo* imaging, and disease treatment.

In addition, one of the core advantages of the sol–gel method is its ability to achieve homogeneous mixing of raw materials at the molecular level, where the precursors form a low-viscosity solution in a solvent, and after hydrolysis, condensation, and other reaction steps, the reactants can achieve homogeneous mixing of molecules at the molecular level during the gel formation stage.[35] Moreover, chemical reactions can be carried out at relatively mild temperatures and atmospheric pressures, and the raw materials and reaction systems used usually do not introduce substances that are harmful to living organisms, making it easy to maintain the biocompatibility of the materials.[36–39] In conclusion, all of the above methods have their own advantages, as well as areas that need to be overcome, but they may not be out of place as viable methods for synthesizing UCNPs.

### 2.4. Alternative methods

In 2022, Yin *et al.* developed a series of $Er^{3+}$-doped ternary sulfide phosphors with efficient UC emission under 1532 nm irradiation.[40] They prepared an MLNS2:$Er^{3+}$ UC phosphor using a gas–solid reaction method. This phosphor was characterized by trivalent rare earth elements (Ln = Y, Lu, La, or Gd) and trivalent metal elements (M = Li, Na, K) occupying the M and Ln positions, respectively.

Upconversion materials with a unique porous structure and loose morphology can be prepared, and this special morphology is conducive to adsorption, diffusion and interaction with the outside world; for example, in some catalytic applications, the porous structure can provide more active sites. Through the full contact and reaction between gas and solid, the surface properties and internal structure of the material can be effectively regulated, thus improving the upconversion luminescence efficiency to a certain extent. However, the prepared morphology is relatively limited to several types of macroscopic morphologies with the characteristics of porous,

loose, *etc.*, and it is difficult to realize fine morphology control at the nanometer level, so it is difficult to meet the needs of applications with stringent requirements on the microscopic morphology of materials, such as nano-bio-imaging. It is difficult to prepare nanoscale upconversion materials with a small and uniform particle size, and their larger particle size determines that they are less suitable for some application scenarios that require materials to interact with biological systems and other fine interactions at the microscopic scale, such as intracellular precision labeling imaging. The homogeneity of a gas–solid reaction is more difficult to ensure, and it is easy to have incomplete local reaction or over-reaction, thus affecting the overall luminescence efficiency and performance consistency of the material, requiring complex process optimization to solve this problem.

# 3. Applications in biology

Conventional probes that utilized excitation and emission bands in the 400–900 nm range suffered from harmful photon scattering, which resulted in suboptimal spatial resolution during the imaging of biological samples. Recent advancements in NIR-II have prompted efforts to shift the excitation wavelength of these nanoparticles from the conventional 980 nm and 808 nm to the spectral range of 1000–1700 nm within the NIR-II window. Upconversion materials in the region offer significant biomedical advantages: (1) *deep tissue penetration* – the NIR-II light wavelengths provide enhanced tissue transparency and deeper penetration into human tissue; (2) *high resolution imaging* – these materials convert radiation into visible or NIR light, enabling high-resolution imaging of biological tissues; (3) *real-time monitoring and diagnostics* – upconversion materials facilitate real-time monitoring of physiological activities and pathological changes in organisms, including tumor marker detection and blood flow observation, supporting early diagnosis and treatment monitoring; (4) *multifunctionality* – these materials not only enable imaging, but also integrate functions like drug delivery and photothermal therapy, enhancing their versatility in biomedical applications. Scientists have explored numerous specialized applications stemming from these advantages, which we will elucidate in the subsequent section.

## 3.1. Featured imaging

The NIR-II window can detect weak autofluorescence and tissue scattering. However, current *in vivo* biological detection with NIR-II fluorophores is limited to disease lesion or organ imaging. Traditional cell imaging relies on fluorophores emitting fluorescence in the visible (400–700 nm) and near-infrared (700–900 nm) ranges. However, tissue autofluorescence and light scattering limit *in vivo* cell tracking,[41] posing a significant challenge for real-time dynamic biosensing in NIR-II.

Liu *et al.* introduced a novel $Er^{3+}$-sensitized upconversion nanoparticle that, when excited at 1530 nm, emits at 1180 nm within the NIR-II window, designed for *in vivo* inflammation biosensing (Fig. 5A).[42] This involved a microneedle patch sensor for dynamic detection of *in vivo* inflammation using fluorescence. The method combines efficient NIR-II upconversion emission with an organic probe for hydrogen peroxide sensing mediated by the $Fe^{2+}$-catalyzed Fenton reaction. Due to NIR-II's low autofluorescence and tissue scattering, luminescence images of microneedle arrays remained clear beneath skin tissue. Single needle signals (200 × 200 μm) were easily distinguishable (Fig. 5C and E). Unlike the stable 1180 nm luminescence (Fig. 5D), the 980 nm signal increased gradually with inflammation progression due to continuous $H_2O_2$ production (Fig. 5C). The linear correlation of log ($I_{980}/I_{1180}$) with $H_2O_2$ concentration (Fig. 5B) indicates that $H_2O_2$ levels at inflammation sites reached 95 μM within 12 hours, consistent with literature reports. This study laid the foundation for the development of high-resolution NIR-II nanoprobes.

Peng *et al.* systematically studied $Tm^{3+}$-doped nanoparticles' emission characteristics under different NIR-II laser excitations.[43] They identified three excitation strategies at 1064 nm, 1150 nm, and 1208 nm, finding that 1150 nm excitation produced 475 nm three-photon emission nearly 100 times stronger than 1064 nm. Post-inert shell incubation further enhanced the luminescence brightness, increasing the emission intensity 10 times. Nanoparticles excited with a 1150 nm laser emitted bright blue light at 475 nm, whereas excitation at 1064 nm and 1208 nm only produced emission at 808 nm (Fig. 5F–H). HeLa cells labeled with hydrophilic UCNPs (20 nm, 1.75% $Tm^{3+}$) and a 5 nm shell were imaged using a 1150 nm laser (Fig. 5I and J). UCNPs were visualized intracellularly under 1150 nm excitation, with cell survival >92% at up to 500 μg $mL^{-1}$ of PAA-coupled $NaYF_4$:Tm@$NaYF_4$ UCNPs, as demonstrated in Fig. 5K. The study suggested that UCNPs have high biocompatibility and minimal toxicity, developing a straightforward NIR-II excitation strategy for cancer cell microimaging.

The absorption of 1064 nm light by fixed mammalian cells is minimal, thereby facilitating confocal imaging without detectable autofluorescence when employing standard continuous-wave lasers. Notably, these lasers have not yet been applied for luminescence imaging of biological samples. In recent years, fluorescence sensors (such as quantum dots and upconversion nanoparticles) had made significant advances in biosensing, but traditional sensors have limited imaging capability in deep tissues due to light absorption and scattering.[44] Elizabeth S. Levy's team used ELNPs excited at non-scattering wavelengths for deep tissue imaging,[45] achieving 2 μm resolution at depths of several millimeters with 5–13 times less signal attenuation than 785 nm-excited UCNPs. To demonstrate the capability to penetrate highly scattering tissue, they employed 1064 nm confocal imaging of energy-looping nanoparticles (ELNPs) for high-resolution imaging through fixed coronal slices of adult mouse brains (Fig. 5L). Small ELNP-loaded beads were distinctly resolved in 1.0 mm thick brain slices, showing 2.0 μm features finer than capillaries. Line cuts of the ELNPs (Fig. 5N) demonstrated no loss in resolution across brain sections during 1064 nm imaging. Their findings

 

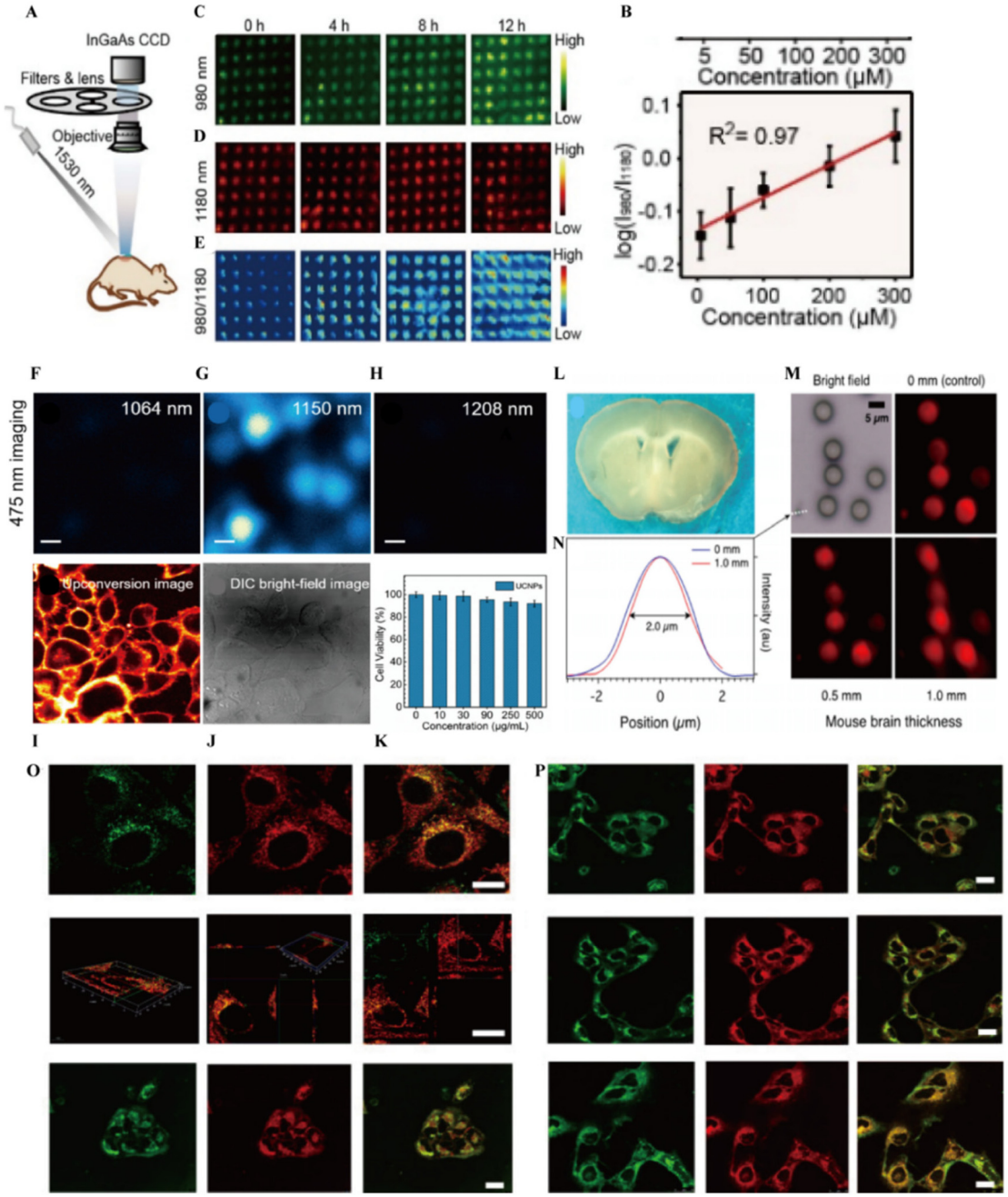


**Fig. 5** (A) Schematic of the *in vivo* bioimaging experimental setup and upconversion luminescence images of microneedle patches at 980 (C) and 1180 nm (D) as well as the ratio ($I_{980}/I_{1180}$) (E) channel.[42] (B) Fluorescence ratios ($I_{980}/I_{1180}$) of microneedle patches for different concentrations of $H_2O_2$.[42] (F) Excitation wavelength: 1530 nm. Multiphoton scanning microscopy images of 475 nm emission from (F–H) $NaYF_4$:Tm (1.75%)@$NaYF_4$ nanoparticles under 1064 nm, 1150 nm, and 1208 nm laser excitation.[43] (I) Upconversion image of HeLa cells treated with $NaYF_4$:Tm (1.75%)@$NaYF_4$ UCNPs. (J) Differential interference contrast (DIC) image.[43] (K) Survival of HeLa cells incubated with different concentrations of $NaYF_4$:Tm (1.75%) @$NaYF_4$ UCNPs for 4 hours.[43] (L) Representative mouse brain sections through which ELNP beads were imaged.[45] (M) Dual-field-of-view and confocal luminescence micrographs of $Tm^{3+}$-doped ELNP beads imaged through 0, 0.5, and 1 mm-thick brain slices, cut along the white dashed line shown in (N) along the line of the measured intensity of the unbound ELNP.[45] (O) All fluorescence images of different concentrations of 3j-PEG, 3k-PEG, H4-PEG or H4-PEG-PT with (P) fluorescence images of commercial mitochondrial dyes (MTR or MTG).[46]

demonstrated that ELNPs, when excited at 1064 nm, facilitate high-fidelity imaging through cellular structures and enable deep brain imaging through tissues with a minimum thickness of 1 mm. This methodology attains imaging depths and feature resolutions that are on par with those achieved through advanced multiphoton techniques.

To date, a few small-molecule NIR-II fluorophores have predominantly utilized donor–acceptor–donor (D–A–D) or sym-

metric structures. Notably, there have been no reports of upconverting mitochondria-targeted NIR-II dyes. Here, Zhou *et al.* developed a thiopyridine NIR-II agent for upconversion imaging and mitochondria-targeted photothermal therapy,[46] showing high precision and ROS-free treatment comparable to commercial dyes. Additionally, the fluorescence intensity was undetectable when the Mitotracker Green concentration was below 10 nM, whereas 1 nM of H4-PEG-PT exhibited a distinct and robust fluorescence signal under identical experimental conditions. NIR-II fluorescence confocal studies (Fig. 5O and P) revealed that 3j-PEG, 3k-PEG, H4-PEG, and H4-PEG-PT were internalized by mitochondria *via* the inner membrane, achieving mitochondrial targeting *via* de-localized lipid-soluble cationic thiopyrrolates rather than through the alkyl triphenylphosphate moiety. In conclusion, H4-PEG-PT thiopyrrole probes enabled targeted NIR-II imaging, cancer diagnosis, therapy, and fluorescence-guided surgery.

All of these examples of featured imaging demonstrate that upconversion materials applied in the NIR2 region have deeper tissue imaging capabilities, higher imaging resolution, and excellent ability to identify, and detect, relevant diseases.

### 3.2. Multimodality imaging

NIR-II upconversion materials can be used for standalone optical imaging and combined with computed tomography (CT), photoacoustic imaging (PAI), and magnetic resonance imaging (MRI) for multimodal imaging, improving tissue structure, function, and metabolism assessment for precise biological insights. NIR-II imaging technology has been combined with photodynamic therapy (PDT) and photothermal therapy (PTT), providing comprehensive anatomical and biological information about the treatment process.[47]

The tumor microenvironment (TME) affects tumor imaging by regulating factors such as hypoxia, pH, GSH, and ROS. Multimodal imaging techniques provide diverse information, enhancing imaging accuracy and reliability.[48] Lv *et al.* proposed using antibodies targeting specific genes alongside rare-earth composites for UCL and DCL near-infrared II imaging to diagnose lung adenocarcinoma (LUAD).[49] They also developed fluorescence imaging probes ($NaYF_4$:Yb, Er, Eu@$NaYF_4$:Nd, referred to as NYF:Eu NPs) with multimodal optical imaging properties. These probes exhibited both DC and UC luminescence within the visible spectrum, as well as luminescence in the NIR-II region. They are characterized by uniform size distribution, improved tissue penetration, and heightened sensitivity. Finally, when combined with antibodies targeting specific genes like TOP2A and CCNB2, the NYF:Eu NP probes can serve as precise optical probes for LUAD diagnosis.

Fig. 6A illustrates NIR-II imaging photographs of Yb, Er@Nd, Yb,Er,Ce@Nd, and Yb,Er,Eu@Nd core/shell nanocrystals in solution under various filters, highlighting NYF:Eu's superior intensity in the NIR-II region. The fluorescence images in Fig. 6B of Balb/c mice bearing 4T1 tumors (left) and A549 tumors (right) reveal NYF:Eu-CCNB2's pronounced signal in A549 cells (signal/background ratio of 4.32) and minimal signal in 4T1 tumors (signal/background ratio of 1.72), indicating promising diagnostic applications for LUAD. Fig. 6C illustrates the application of NIR-II imaging-guided lung nodule

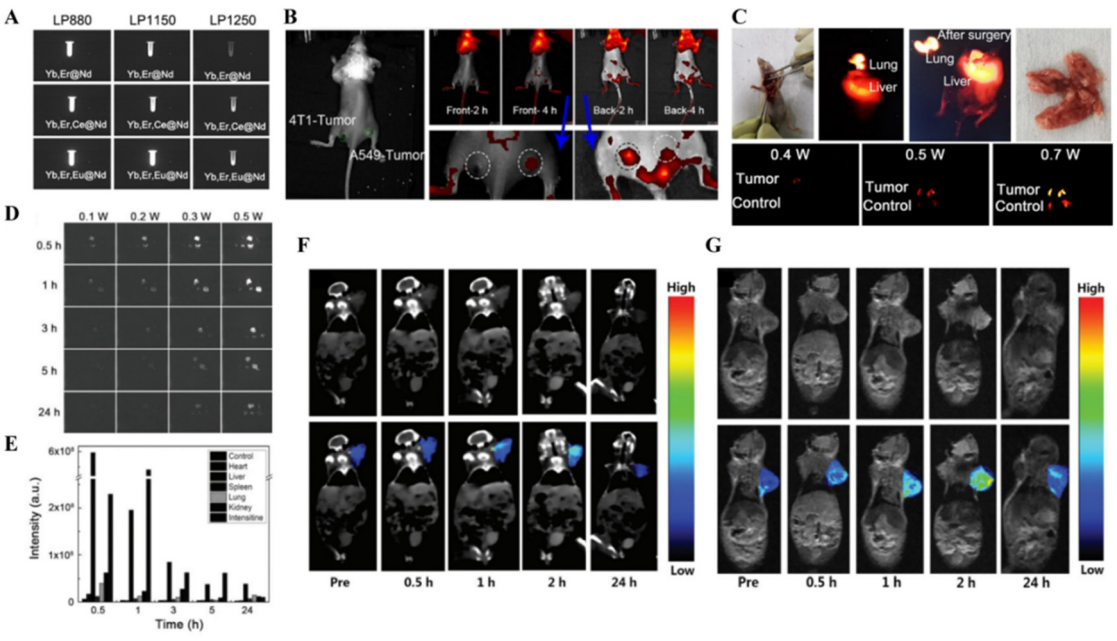


**Fig. 6** (A) NIR-II imaging photographs of the core/shell nanocrystals under different filters. (B) *In vivo* fluorescence imaging photograph of the mouse grown with 4T1 and A549 tumor cells intravenously injected with NYF:Eu-CCNB2. (C) *In situ* surgery navigation.[49] (D) NIR-II imaging photographs. (E) The corresponding quantitative analysis results of mouse organs after injection through the tail vein at different time points.[50] (F) Time-dependent CT imaging in tumor-bearing mice before and after intravenous injection of the UCNPs-$Cu_{2-x}S$ nanocomposites. (G) Time-dependent MR imaging in tumor-bearing mice before and after intravenous injection of the UCNP-$Cu_{2-x}S$ nanocomposites.[51]

 

surgery in mice. Without NIR-II imaging, visualizing lung nodules was challenging (mice were intravenously injected with A549 cells for about one week). Twenty minutes post-injection of the NYF:Eu-TOP2A nanoprobe, lungs with cancer cells exhibited significantly higher luminescence than the liver, demonstrating greater nanoprobe uptake than in cancer-free lungs. This suggested its potential for precise diagnosis and surgical guidance to differentiate between tumor and normal tissue in the future. This strategy of antibody-conjugated optical probes offers a bimodal luminescence imaging approach for precision medicine.

Lin and colleagues developed bimodal optical imaging probes using rare earth nanoparticles (RENPs) functionalized with peptides.[50] They enhanced red UCL and NIR-II imaging intensities in RENP@C@Au (UCA) through metal and co-dopant adjustments. Next, cMBP peptides, which targeted Cal 27 TSCC cells expressing high levels of c-MET protein, were conjugated to UCA. These probes were specifically designed for imaging and therapeutic applications against Cal 27 cells, distinguishing them from other cell lines including normal human cells (MCF-10A, A549, HeLa) and mouse 4T1 tumor cells.

Two fluorescence imaging methods were employed: in the visible region and in the near-infrared region. Advantages include enhanced information for reflecting the final distribution and improved stability of the imaging method due to natural fluorescence of the probes (eliminating dye–carrier separation). Fig. 6D demonstrates that the distribution of UCA-cMBP in the liver and intestine of mice reached its maximum at 0.5 h when subjected to different power settings of the NIR-II imaging device. *In vivo* biodistribution exhibited a declining trend over time, reaching a minimum at 24 h. Fig. 6E illustrates the distribution of RENP-cMBP in the liver and intestine using NIR-II imaging. The data indicate that the concentration of RENP-cMBP in the liver and intestine of mice reached its maximum at 0.5 hours post-administration, followed by a subsequent decline in fluorescence intensity over time. At 5 h, liver and intestinal tissues exhibited minimal fluorescence, consistent with NIR-II small animal imaging results.

Du *et al.* proposed and designed a novel multifunctional nanoplatform using $Cu_{2-x}S$ conjugated $NaYF_4$:Yb/Er@$NaYF_4$:Yb upconversion nanoparticles.[51] The UCNPs in the UCNPs–$Cu_{2-x}S$ nanocomposites exhibited excellent luminescence properties and high X-ray attenuation coefficients, thereby facilitating their application as UCL and CT imaging contrast agents. Additionally, Cu(II) in the $Cu_{2-x}S$ nanodots imparted MRI capability to the nanocomposites due to its unpaired electrons. The high photothermal conversion efficiency (43.8%) at 1064 nm in the near-infrared-II biological window indicated significant potential for synergistically enhancing UCL/CT/MR multimodal imaging-guided CDT/PTT cancer therapy.

The CT signal at the tumor site showed significant enhancement within 2 hours as depicted in Fig. 6F, attributed to an improved EPR (permeability and retention) effect. Subsequently, CT signals at the tumor site notably diminished 24 hours post-injection, indicating gradual clearance of UCNPs–$Cu_{2-x}S$ nanocomposites from mice. These findings highlighted the potential of UCNPs–$Cu_{2-x}S$ nanocomposites as effective *in vivo* CT contrast agents. In Fig. 6G, following intravenous administration of UCNPs–$Cu_{2-x}S$ nanocomposites, MR signals at the tumor site exhibited progressive enhancement within 2 hours. Later, metabolic processes led to signal attenuation within 24 hours, consistent with CT imaging observations. This multimodal imaging approach showed promise as a bioimaging probe.

A growing number of articles have shown that by combining NIR-II imaging with clinical imaging techniques, as well as PDT and PTT, a greater degree of better anatomical information, a more comprehensive view of the treatment process, and more enriched biological information can be provided.

### 3.3. Assistance for disease treatment

Methicillin-resistant *Staphylococcus aureus* (MRSA) forms stable biofilms, leading to antibiotic resistance and severe health threats. The bacteria aggregate tightly through extracellular polymeric substances (EPS), enhancing resistance and causing wound inflammation, especially in diabetic patients. Lanthanide-doped upconversion luminescent materials (UCLMs) convert NIR-II light to ultraviolet (UV)/blue light, overcoming the limitations of traditional materials in deep infections.

For example, Wang *et al.* developed a $NaYF_4$:$Yb^{3+}$/$Tm^{3+}$@$NaYF_4$ three-layer core–shell upconversion luminescent material (US) with a dendritic silica coating.[52] Surface amination modification was performed to enhance its anionic drug loading and bacterial adhesion (Fig. 7A). The US not only exhibited substantial porosity and high drug-loading capacity, but also demonstrated effective conversion of NIR-II light to UV light. The antimicrobial efficacy was evaluated at different concentrations of antimicrobial agents, in both the presence and absence of NIR irradiation, over a time span ranging from 0 to 12 minutes (Fig. 7B and C). Building on this, they synthesized KCD-modified US (USK) and filled it with the NO precursor BNN6 (*N*,*N*′-di-*sec*-butyl-*N*,*N*′-dinitroso-1,4-phenylene diamine) to create USKB. *In vitro* antimicrobial assays demonstrated that USKB exhibited significant antibacterial activity when activated by NIR-II light (Fig. 7D and E). Additionally, *in vivo* studies indicated that USKB, under NIR-II activation, facilitated the healing of diabetic wounds (Fig. 7F). Mechanistic studies indicated that USKB produces three types of ROS under NIR-II light, effectively exhibiting antimicrobial activity by disrupting MRSA's antioxidant systems, inhibiting bacterial ATP synthesis, and degrading biofilms.

Tumor imaging and image-guided surgery often fail in treating solid tumors due to local recurrence. The main treatments include surgery, chemotherapy, and radiotherapy, but chemotherapy and radiotherapy suffer from a lack of precise targeting, high levels of side effects, and difficulty in maintaining efficacy. Imaging technology leads diagnosis and treatment, while NIR-II imaging (1000–1700 nm) provides high-

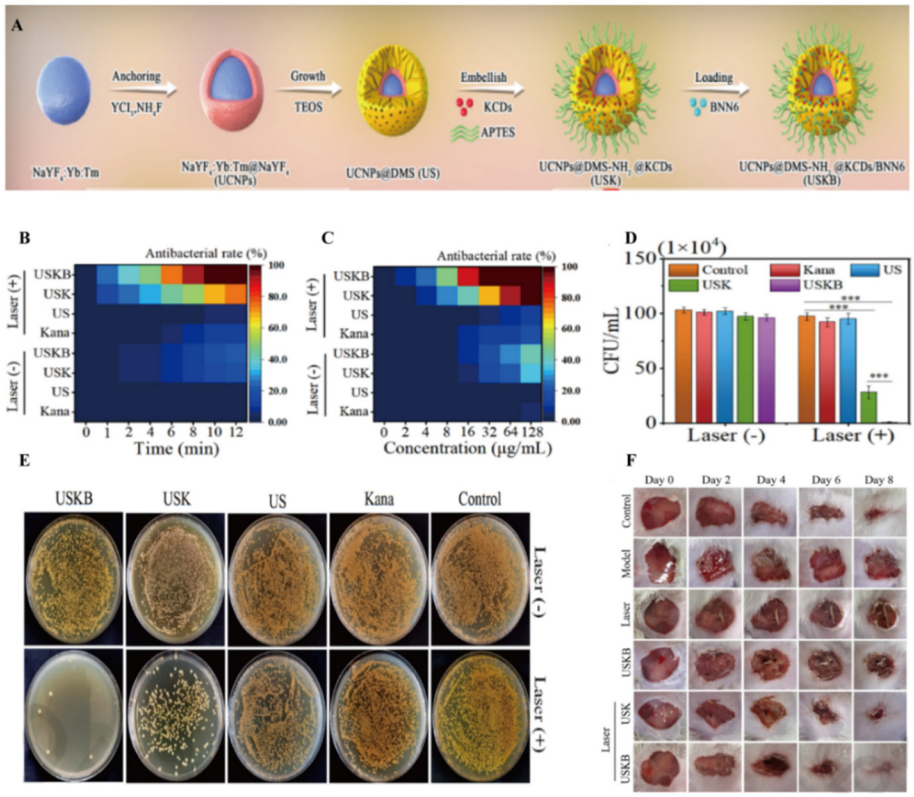


**Fig. 7** (A) Synthesis route to USKB against MRSA biofilm infection in diabetic wounds.[52] (B) Time-dependent or concentration-dependent. (C) Antimicrobial activity of Kana, US, USK, and USKB after 10 min with or without laser treatment (980 nm, 1 W $cm^{-2}$).[52] (D) Antimicrobial efficiencies of Kana, US, USK and USKB with and without laser treatment examined by the CFU method and are represented as colony counting results and typical representative images of CFU (E).[52] (F) Photographs of biofilm-infected wounds in the USKB group ($n$ = 6) with and without laser treatment from day 0 to day 8.[52]

resolution, real-time imaging, supporting the evaluation of superficial tumors and chemotherapy effectiveness.

For example, Wang *et al.* designed functionalized core–shell rare earth nanoparticles (ORENPs) for tumor localization during image-guided tracking.[53] When dealing with triple-negative breast cancer (TNBC) that presents a complex microenvironment and lacks target sites, medication was administered through two pathways encapsulated in the "light-cleaving band". Specifically, the assembly mechanism is illustrated in Fig. 8A, where ORENPs emit NIR-II light, while enabling energy upconversion to emit UV light for drug release and MC stimulation. Due to the highly PEGylated surface of ORENPs, they exhibit good blood circulation, and even with low accumulation at the tumor site, NIR-II imaging (808/NIR-II) is possible (Fig. 8B). Once the presence of ORENPs near the tumor tissue has been confirmed, the light source can be switched to precisely release CP 48/80, activating tumor-infiltrating mast cells (MCs). The results indicated that precisely activating tumor-infiltrating MCs can overcome barriers of tumor blood vessels and the extracellular matrix, leading to higher nanoparticle absorption at tumor sites while avoiding toxicity to normal tissues, offering a new option for treating TNBC cancer. Ultimately, the integrated application of chemical and cellular methodologies facilitates a substantial increase in tumor infiltration by clinical nanomedicines, thereby augmenting the efficacy of nanochemotherapy.

In most solid tumors, the distortion of the tumor vasculature and significant oxygen consumption caused by abnormal tumor proliferation lead to a hypoxic environment, defined as hypoxia. Tumor hypoxia occurs early in tumor development, and alleviating hypoxia and reducing oxygen consumption are effective strategies to enhance the efficacy of photodynamic therapy.[54] To achieve precise therapy, it is crucial to monitor the accumulation of nanomedicines and determine the optimal PDT triggering time.

For example, Li *et al.* proposed an acid-responsive NIR-II fluorescence imaging-guided smart nanomedicine LDNP@$SiO_2$–$CaO_2$ and folic acid (FA)–polyethylene glycol (PEG)-Ce6 (LSCaFPCe6) to address tumor hypoxia and systemic toxicity issues during PDT (Fig. 8C).[55] $Nd^{3+}$ in LDNPs was used for NIR-II fluorescence imaging to monitor nanoparticle delivery, tumor accumulation, and optimal triggering times. $Er^{3+}$ exhibited significant upconversion luminescence during PDT, serving as the excitation source for Ce6 (Fig. 8D). A dendritic silica layer on LDNPs facilitated the synthesis of ultrafine calcium peroxide, forming rough-surfaced nano-composite materials (LSCa). The FA-PEG-Ce6 polymer was further coated on LSCa nanocomposites to produce LSCaFPCe6. When

 

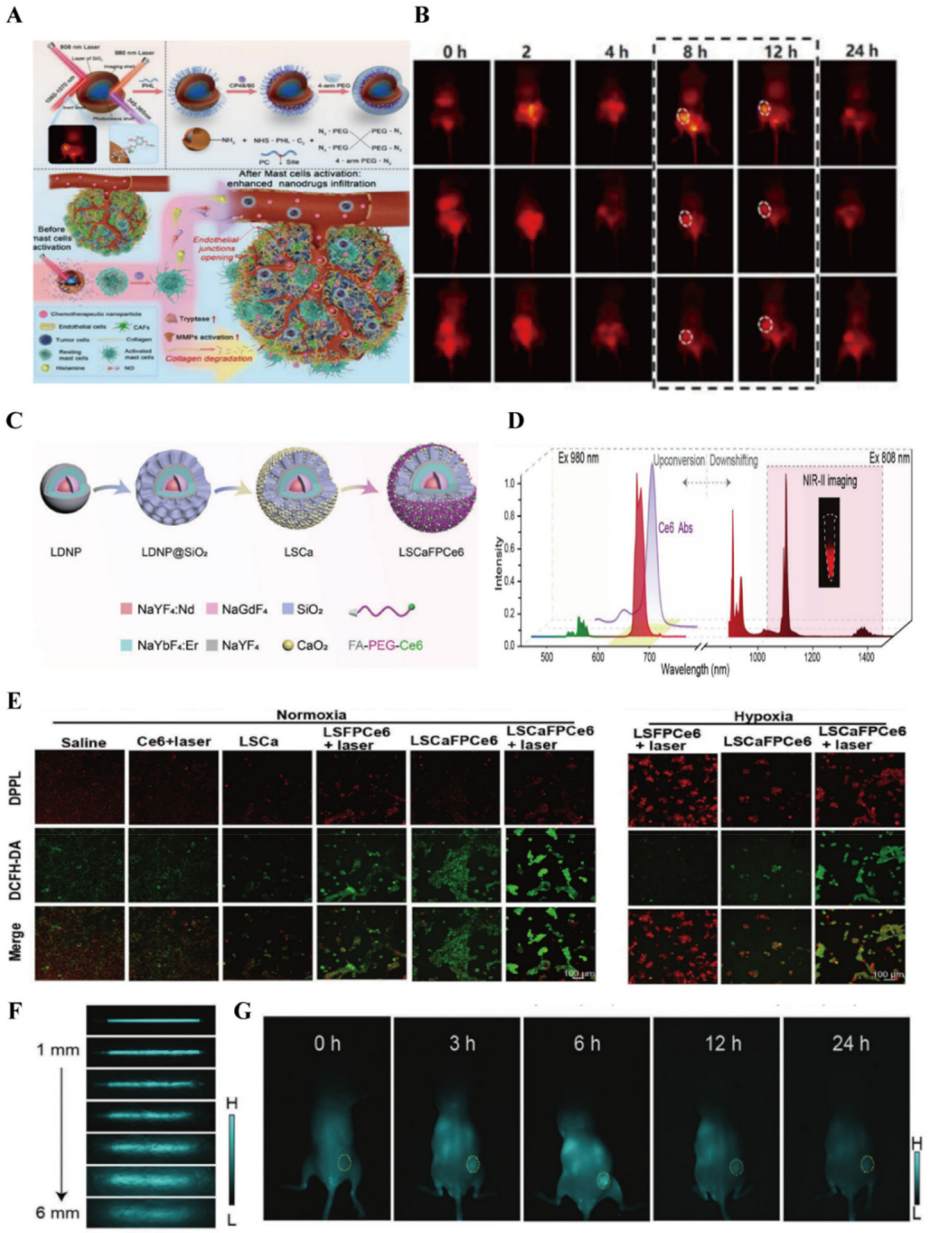


**Fig. 8** (A) Schematic diagram of the dual NIR excitation used to construct ORENP and its corresponding up/down conversion emission and application for effective cancer nanochemotherapy.[53] (B) NIR-II imaging of OCP in a 4T1 orthogonal anisotropic tumor model.[53] (C) Fabrication of LSCaFPCe6 nanodrugs.[55] (D) Ce6 absorbance and upconversion/downshift emission spectra of LDNP under 980 and 808 nm excitation, respectively.[55] (E) CLSM observations of cellular ROS and $O_2$ levels in 4T1 cells.[55] (F) NIR-II fluorescence imaging of capillaries at different depths in pork tissue.[55] (G) *In vivo* NIR-II fluorescence imaging of the nude mice with PC3 tumor after intravenous (i.v.) injection of LSCaFPCe6 (10 mg $kg^{-1}$) at different time points after injection.[55]

exposed to the acidic TME LSCaFPCe6 released large amounts of $O_2$, $H_2O_2$, and $Ca^{2+}$ ions, alleviating tumor hypoxia and enhancing the PDT efficacy and $Ca^{2+}$-mediated apoptosis (Fig. 8E). NIR-II fluorescence imaging was used to tracke nanomedicines, detecting signals at 6.0 mm depth despite tissue scattering (Fig. 8F). The tumor site fluorescence intensity peaks at 6 hours before decreasing (Fig. 8G). This method not only mitigated hypoxia in the TME to improve PDT effectiveness, but also allowed optimal triggering time to be determined through secondary NIR-II fluorescence imaging. The results showed that functional LSCaFPCe6 nanoparticles effectively supply $O_2$, $H_2O_2$, and $Ca^{2+}$, alleviating intracellular hypoxia and enhancing ROS and $Ca^{2+}$-mediated apoptosis, thereby improving anticancer activity. The NIR-II imaging-guided TME-responsive PDT nanoparticle system demonstrated enhanced antitumor efficacy with no significant systemic toxicity.

These publications not only demonstrate the excellent imaging properties of upconverted materials in NIR-II, but also show that they play an important role in assisting in the

treatment of various diseases, with capabilities such as anti-inflammatory and antibacterial, assessing the accumulation time of drugs in the body, and the ability to produce superficial chemotherapeutic effects.

### 3.4. Integrated diagnostics and therapeutics

Breast cancer is a primary cancerous growth that presents a major danger to women's well-being. TNBC lacks specific molecular markers and targeted therapeutic drugs, leading to high malignancy, high metastasis rate, and low survival rate, making it a global health issue.

For example, Wang *et al.* developed ZUPEA nanoparticles using a double-emulsion method with PEG-PLGA and ultrafine RE nanoparticles (RENPs) incorporating the photosensitizer ZnPc.[56] A schematic of the designed probe is shown in Fig. 9A. These nanoparticles, exhibiting effective PDT *in vitro*, degraded into small particles (<6 nm). Modified with the cMBP peptide, they targeted MDA-MB-231 TNBC cells *via* positive MET imaging and EPR effects. The nanospheres improved the drug loading efficiency and reduced loss, enhancing the final cytotoxic effect. Additionally, after completing the therapeutic diagnostic process at the lesion site, the ultrasmall RENPs could be excreted from the body through the kidneys. Under NIR laser irradiation, a photodynamic reaction was triggered, producing ROS to inhibit tumor cell growth through upconverted red light emission. NIR-II imaging aided in better tumor identification, successfully implementing integrated diagnosis and therapy (Fig. 9B). This specially designed ZUPEA probe, integrating diagnostic and therapeutic functions, provides new ideas and prospects for the application of rare earth nanoparticles in clinical cancer treatment.

Cai *et al.* synthesized RE nanoprobes *via* co-precipitation and developed rare earth nanoparticles conjugated with dihydroartemisinin (DHA) and targeting antibodies (-DHA-Cap) for NIR-II imaging and PDT in tongue cancer spray applications (Fig. 9C).[57] Using genetic algorithms to guide the concentration of sensitizers and activators, T1 MRI signals could be adjusted through Gd ion concentrations. The optimized RENP conjugated with DHA exhibited excellent *in vivo* NIR-II luminescence and superb PDT efficacy under 980 nm irradiation (Fig. 9D and E). Combined with a targeted antibody against carmustine (Cap), this allowed for precise NIR-II imaging

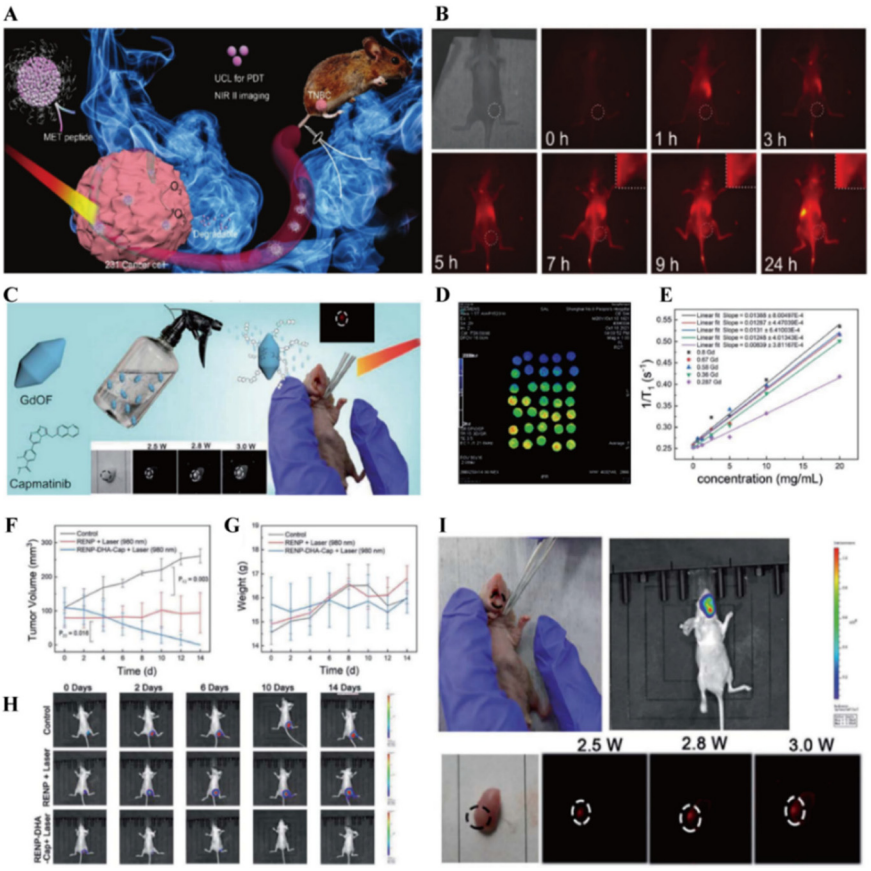


**Fig. 9** (A) Schematic of the designed probe.[56] (B) NIR-II imaging of mice with TNBC tumors after tail vein injection of ZUPEA-cMBP.[56] (C) Schematic of the designed nanoparticles and biological use for luminescence imaging of tongue cancer.[57] (D) T1 mapping images of MRI, and (E) relationship between T1 relaxation rate and sample concentration at different Gd concentrations.[57] (F) Change curves of tumor volume and (G) body weight during 14-day treatment and (H) bioimaging images of Luc-labeled Cal 27 tumor cells in mice.[57] (I) NIR-II imaging of mice with *in situ* tumors after treatment with RENP-DHA-Cap spray.[57]

 

(Fig. 9I) and therapeutic capabilities (Fig. 9F–H) for tongue cancer *in situ* through a simple spray method. The results showed that RENP conjugated with DHA demonstrated excellent PDT efficacy. Furthermore, the synthesis of RENP-DHA-Cap imparted targeting capabilities to the probe. The RENP-DHA-Cap probe demonstrated efficacy for *in situ* imaging in both *in vivo* and *in vitro* experiments. This orthogonal diagnostic and therapeutic approach, offering precise diagnosis and targeted treatment, could advance the field of tongue cancer treatment and diagnosis. All of these show the powerful functions of NIR-II region upconversion materials, and the materials integrating diagnostics and therapeutics will have broader application scenarios and more significant clinical value.

### 3.5. Temperature sensing

NIR-II upconversion nanomaterials are receiving increasing attention for applications in temperature sensing. Transforming low-energy near-infrared radiation into high-energy visible light, these substances enable extremely precise temperature measurements. A clear relationship exists between their luminous intensity and temperature changes, allowing temperature changes to be accurately monitored.

It is the first time that $NaErF_4$:$Tm^{3+}$@$NaYF_4$ core–shell nanoparticles have been used in the development of an optical temperature sensor based on cellulose fibers. $NaErF_4$:$Tm^{3+}$@$NaYF_4$ UCNPs exhibited a strong up-conversion upon excitation with 1532 nm near-infrared light,[58] which was attributed to the presence of $Er^{3+}$ in their structure. $Tm^{3+}$ played a particularly intriguing role in UC mechanisms. The addition of $Tm^{3+}$ effectively transforms the typical green UC of $Er^{3+}$ to red, which is particularly needed in anti-counterfeiting applications.

$NaErF_4$:$Tm^{3+}$@$NaYF_4$ nanoparticles were incorporated into cellulose fibers as luminescent modifiers without altering their physicochemical properties. Upon excitation with a 1532 nm near-infrared (NIR) laser, the cellulose fibers exhibited bright red luminescence. The emission spectra of $Er^{3+}$ were dominated by $^4F_{9/2} \rightarrow {}^4I_{15/2}$ (660 nm) and $^4I_{9/2} \rightarrow {}^4I_{15/2}$ (810 nm) at the 1532 nm excitation wavelength. Fig. 10A illustrates the emission spectra of cellulose fibers recorded within the temperature range of 296–473 K. The higher the temperature, the weaker the observed emission. Two bands of emission from the fiber, $^2H_{11/2} \rightarrow {}^4I_{15/2}$ and $^4S_{3/2} \rightarrow {}^4I_{15/2}$, exhibited good sensing performance under 1480 nm excitation, which was temperature dependent. The nature of the synthesized

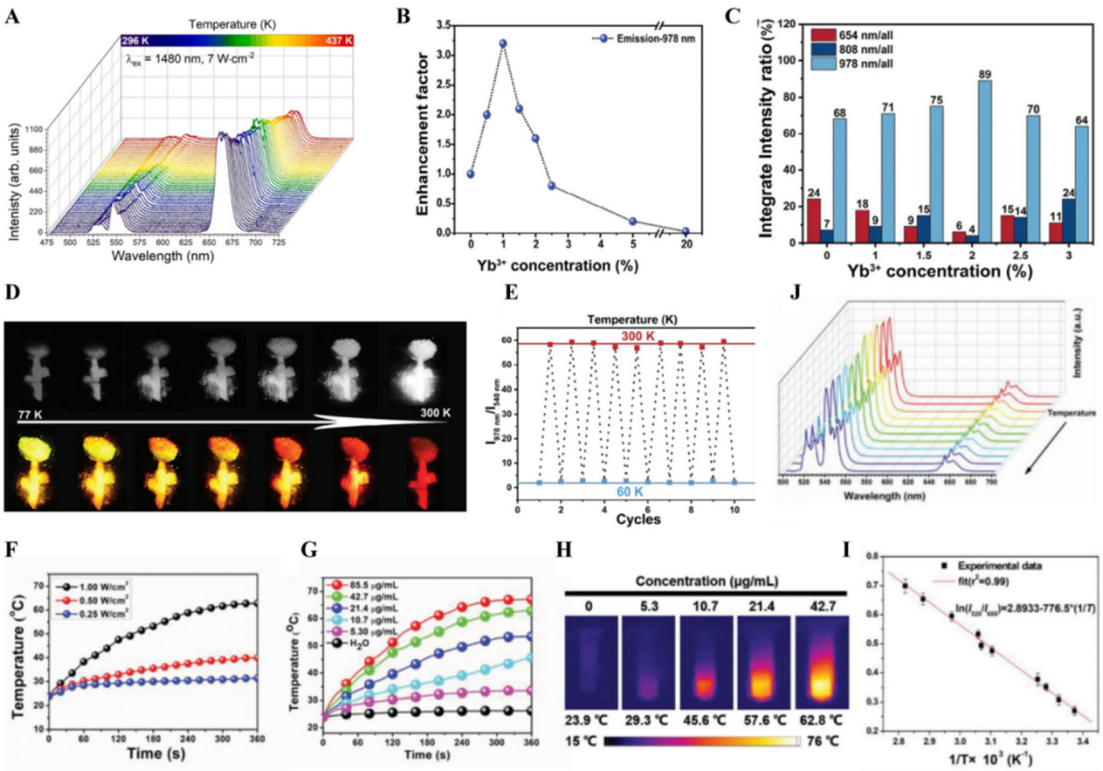


**Fig. 10** (A) Dependence of upconversion luminescence on temperature recorded for cellulose fibers under 1480 nm excitation.[58] (B) The emission intensity enhancement factor under 1532 nm excitation (0.455 W $cm^{-2}$). (C) The intensity ratio of different UCNPs upon 1532 nm excitation (0.455 W $cm^{-2}$). (D) $NaErF_4$:2%Yb@$NaYF_4$ imaging effects under excitation at 1532 nm (up), and display effect diagrams of visible light (down). (E) Cycle stability test of $NaErF_4$:2%Yb@$NaYF_4$. (F) Temperature curves of UCILA upon different 1064 nm laser densities.[59] (G) Temperature increases of different concentrations of UCILA upon 1064 nm laser irradiation. (H) Thermal imaging of UCILA solution at different concentrations upon 1064 nm laser irradiation for 6 min. (I) A plot of in ($I_{520}/I_{655}$). (J) UCL spectra of UCILA at different temperatures (from 20 to 80 °C) by external heating.[61]

cellulose fibers allowed them to be used as optical temperature sensors.

Liu and colleagues presented monochromatic $Er^{3+}$ rich ($NaErF_4$:*x*%Yb@$NaYF_4$) nanoparticles with an excitation wavelength of 1532 nm and an emission wavelength of 978 nm.[59] The authors studied the UCL spectra (1532 nm excitation) for different $Yb^{3+}$ concentrations (0–20%) ($NaErF_4$:*x*%Yb@$NaYF_4$), and the luminescence intensity was increased by up to a factor of 3.2 when doped with a low concentration of $Yb^{3+}$ in $NaErF_4$ compared to undoped UCNPs, due to the effective CR and ET between Er–Yb–Er (Fig. 10B). However, the UC intensity, particularly for visible and NIR-I emission, decreased sharply with higher $Yb^{3+}$ doping of UCNPs (>1%). At a doping concentration of 2% $Yb^{3+}$, it exhibited a NIR-II monochromatic emission efficiency of 89%, accompanied by minimal visible light emission (Fig. 10C). These results indicated that $Yb^{3+}$ doping affected the luminescence of different energy levels to different degrees, suggesting UCNPs with potential NIR-II monochromatic emission. More interestingly, the energy exchange between $Er^{3+}$ and $Yb^{3+}$ can be limited at lower temperatures. The CR became more prominent as the temperature increased. This phenomenon allowed the luminescence signal to be converted to a temperature value, as demonstrated in luminescence display tests under low-power excitation at different temperatures. This study developed a formula to determine temperature from luminescence intensity ratios, enabling its use in temperature sensing applications.

On the basis of the thermal visible light and NIR UCL properties, the authors fabricated flowerlet shapes using $NaErF_4$:2%Yb@$NaYF_4$ UCNPs for thermal sensing and NIR-II invisible tampering applications (Fig. 10D). Increasing the temperature from 77 K to 300 K resulted in a significant increase in NIR spectrum intensity, which resulted in the flower turning from green to red as its color gradually changed. For testing the reusability of the material, UCNPs were repeatedly tested at low temperature and at room temperature, with the luminescence intensity integrals not changing significantly after numerous repetitions (Fig. 10E). As shown in the study, the material has good prospects for use in ultra-low temperature measurements as well as room temperature measurements. In addition, the $Yb^{3+}$ doped UCNPs demonstrated exceptional stability and reversibility, as illustrated in Fig. 10E. This indicates their potential as a robust and efficient material for non-contact cryogenic sensing applications within the field of cryogenic engineering.

PTT has shown its superiority in cancer treatment, including a controlled treatment process and high eradication efficiency. However, PTT can cause damage to normal tissues in the process of killing tumor cells using the tremendous heat generated by photothermal agents. Real-time imaging of these temperatures reveals heat gradients and regulatory mechanisms, enhancing the understanding of cellular functions and organelles.[60] For the real-time sensing/monitoring of microscopic temperature variations during PTT, temperature feedback photothermal agents are indispensable. Xu *et al.* developed an innovative NIR-II theranostic nanoplatform that integrates UCNPs and IR-1048 dye (NIR-II, 1000–1700 nm) within lipid aptamer nanostructures (UCILA).[61] The fluorescence intensity of the UCILA exhibited a positive correlation with its photothermal temperature, thereby facilitating precise monitoring of both photothermal therapy and photothermal imaging (PTI) temperatures accurately.

To elucidate the photothermal properties of UCILA, the researchers conducted an experiment wherein they measured temperature variations following the irradiation of five groups of UCILA solutions at varying concentrations, with pure water serving as the control group. These solutions were exposed to 1064 nm lasers at different power densities (0.25, 0.5, and 1.0 W $cm^{-2}$) for a duration of 6 minutes. As illustrated in Fig. 10F, UCILA exhibited a pronounced NIR-II laser power-dependent effect. Furthermore, Fig. 10G demonstrates that the temperature increased significantly with higher UCILA concentrations, reaching up to 45.5 °C, in stark contrast to the 7.1 °C observed for pure water. The concentration-dependent photothermal effect is further illustrated by the NIR-II thermal image in Fig. 10H. In addition to PTI, which served to monitor the macroscopic temperature at the tumor site, thermal upconversion UCL was also capable of detecting microscopic temperature variations within UCILA. Experimental observations, as illustrated in Fig. 10I and J, revealed a linear relationship in the UCL spectra of UCILA across varying temperatures. Consequently, UCL demonstrated the ability to detect temperature fluctuations during PTT. The integration of precise microscopic temperature monitoring of UCILA *via* UCL, alongside the macroscopic temperature assessment provided by PTI, is expected to enhance the overall accuracy of PTT. This dual approach aims to optimize therapeutic outcomes while mitigating the risk of thermal damage to adjacent healthy tissues and cells. NIR-II upconversion nanomaterials excel in temperature measurement applications. Not only the amount of dopant ions affects the luminescence and energy exchange, which can be converted to temperature, but also the nanoparticles can be used in cellulose fiber optical temperature sensors whose luminescence intensity varies with the temperature and can be used to monitor different temperatures. It is also possible to synthesize different nanoplatforms that can monitor micro and macro temperature changes in photothermal therapy by fluorescence intensity, improving the accuracy of PTT.

## 4. Conclusion

This review summarizes recent advancements in NIR-II upconversion nanomaterial research, focusing on synthesis, optimization, and diverse applications. These nanoparticles have emerged to meet increasingly complex application demands and hold great potential for future research. In the past decade, researchers have succeeded in synthesizing nanoparticles with controllable shapes, sizes, morphologies, and physical phases. The successful fabrication of high-quality nanoparticles has expanded their applications in tumor diag-

 

nosis and therapy, *in vivo* bioimaging, and *in vitro* environmental sensing and detection.

Despite these achievements, several challenges remain to be addressed:

1. *Low upconversion efficiency*: low efficiency in upconversion processes calls for optimized synthetic approaches to enhance photon absorption, energy transfer, and emission.

2. *Poor conversion stability*: advancing surface modification and functionalization to enhance antioxidant, magnetic, and thermal stability.

3. *High toxicity*: enhancing biocompatibility and degradability by reducing the rare earth content and particle size and exploring rapid organ clearance to minimize long-term cytotoxicity.

Overall, NIR-II upconversion nanomaterials show great potential in the biomedical field, but still face many limitations and challenges that require more in-depth research. Continued innovations in materials chemistry, photophysics, and biology will expand the applications of NIR-II upconversion nanoparticles. They promise advancements in biosensing, noninvasive molecular imaging, effective therapeutics, targeted drug and gene delivery, and light-controlled personalized disease treatments. Materials like these have tremendous potential, warranting further comprehensive research and development.

## Author contributions

Conceptualization, investigation, and writing – original draft: Luo R. R., Zhang C. X., and Zhang Z. N. contributed equally to this work. Writing: Ren P. C. Writing – review & editing, supervision, and funding acquisition: Liu Y., Xu Z. S.

## Data availability

This is a review paper, there are no data issues.

## Conflicts of interest

There are no conflicts to declare.

## Acknowledgements

Zhongsheng Xu is thankful the Natural Science Foundation of Chongqing (CSTB2024NSCQ-MSX0394). Yun Liu thanks the Senior Medical Talents Program of Chongqing for Young and Middle-aged, Chongqing Returned Overseas Students' Entrepreneurship and Innovation Support Program (cx2021006), the CQMU Program for Youth Innovation in Future Medicine (W0171), the Kuanren Doctoral supervisor Cultivation Program of the second affiliated hospital of Chongqing Medical University and the Kuanren Talents Program of the second affiliated hospital of Chongqing Medical University.

## References

1 X. Cheng, J. Zhou, J. Yue, Y. Wei, C. Gao, X. Xie and L. Huang, *Chem. Rev.*, 2022, **122**, 15998–16050.
2 X. Zhu, J. Zhang, J. Liu and Y. Zhang, *Adv. Sci.*, 2019, **6**, 1901358.
3 M. Matulionyte, A. Skripka, A. Ramos-Guerra, A. Benayas and F. Vetrone, *Chem. Rev.*, 2022, **123**, 515–554.
4 Du K, Feng J, Gao X and H. Zhang, *Light: Science & Applications*, 2022, **11**, 222.
5 M. Wang, C. Mi, Y. Zhang, J. Liu, F. Li, C. Mao and S. Xu, *J. Phys. Chem. C*, 2009, **113**, 19021–19027.
6 J. F.-C. Loo, Y.-H. Chien, F. Yin, S.-K. Kong, H.-P. Ho and K.-T. Yong, *Coord. Chem. Rev.*, 2019, **400**, 213042.
7 J. Zhou, Q. Liu, W. Feng, Y. Sun and F. Li, *Chem. Rev.*, 2015, **115**, 395–465.
8 Y. Wei, Z. Cheng and J. Lin, *Chem. Soc. Rev.*, 2019, **48**, 310–350.
9 S. Wen, J. Zhou, K. Zheng, A. Bednarkiewicz, X. Liu and D. Jin, *Nat. Commun.*, 2018, **9**, 2415.
10 Y. Ma, M. Song, L. Li, X. Lao, M.-C. Wong and J. Hao, *Exploration*, 2022, **2**, 20210216.
11 S. Mallidi, S. Anbil, A.-L. Bulin, G. Obaid, M. Ichikawa and T. Hasan, *Theranostics*, 2016, **6**, 2458.
12 J. Zhao, D. Zhong and S. Zhou, *J. Mater. Chem. B*, 2018, **6**, 349–365.
13 Z. Liu, S. Tabakman, K. Welsher and H. Dai, *Nano Res.*, 2009, **2**, 85–120.
14 Z. Lei and F. Zhang, *Angew. Chem., Int. Ed.*, 2021, **60**, 16294–16308.
15 Y.-W. Zhang, X. Sun, R. Si, L.-P. You and C.-H. Yan, *J. Am. Chem. Soc.*, 2005, **127**, 3260–3261.
16 F. Wang, R. Deng and X. Liu, *Nat. Protoc.*, 2014, **9**, 1634–1644.
17 J. Huang, J. Li, X. Zhang, W. Zhang, Z. Yu, B. Ling, X. Yang and Y. Zhang, *Nano Lett.*, 2020, **20**, 5236–5242.
18 Q. Feng, W. Zheng, J. Pu, Q. Chen and W. Shao, *Front. Chem.*, 2021, **9**, 690833.
19 G. Yi, H. Lu, S. Zhao, Y. Ge, W. Yang, D. Chen and L.-H. Guo, *Nano Lett.*, 2004, **4**, 2191–2196.
20 S. Han, A. Samanta, X. Xie, L. Huang, J. Peng, S. J. Park, D. B. L. Teh, Y. Choi, Y. T. Chang and A. H. All, *Adv. Mater.*, 2017, **29**, 1700244.
21 C. D. S. Brites, X. Xie, M. L. Debasu, X. Qin, R. Chen, W. Huang, J. Rocha, X. Liu and L. D. Carlos, *Nat. Nanotechnol.*, 2016, **11**, 851–856.
22 Q. Chen, X. Xie, B. Huang, L. Liang, S. Han, Z. Yi, Y. Wang, Y. Li, D. Fan and L. Huang, *Angew. Chem.*, 2017, **129**, 7713–7717.
23 X. Cheng, Y. Pan, Z. Yuan, X. Wang, W. Su, L. Yin, X. Xie and L. Huang, *Adv. Funct. Mater.*, 2018, **28**, 1800208.
24 T. Peng, R. Pu, B. Wang, Z. Zhu, K. Liu, F. Wang, W. Wei, H. Liu and Q. Zhan, *Biosensors*, 2021, **11**, 148.
25 X. Wang, J. Zhuang, Q. Peng and Y. Li, *Nature*, 2005, **437**, 121–124.

26 G. Zhang, Y. Yang, J. Shi, X. Yao, W. Chen, X. Wei, X. Zhang and P. K. Chu, *Biomaterials*, 2021, **269**, 120634.
27 K. de Oliveira Lima, L. F. Dos Santos, R. Galvão, A. C. Tedesco, L. de Souza Menezes and R. R. Gonçalves, *Front. Chem.*, 2021, **9**, 712659.
28 K. Du, J. Feng, X. Gao and H. Zhang, *Light: Sci. Appl.*, 2022, **11**, 222.
29 M. A. Boles, M. Engel and D. V. Talapin, *Chem. Rev.*, 2016, **116**, 11220–11289.
30 Z. Zhang, Y. Chen and Y. Zhang, *Small*, 2022, **18**, 2103241.
31 D. Yang, J. Han, Y. Sang, T. Zhao, M. Liu and P. Duan, *J. Am. Chem. Soc.*, 2021, **143**, 13259–13265.
32 N. J. Greybush, M. Saboktakin, X. Ye, C. Della Giovampaola, S. J. Oh, N. E. Berry, N. Engheta, C. B. Murray and C. R. Kagan, *ACS Nano*, 2014, **8**, 9482–9491.
33 Z. Yuan, L. Zhang, S. Li, W. Zhang, M. Lu, Y. Pan, X. Xie, L. Huang and W. Huang, *J. Am. Chem. Soc.*, 2018, **140**, 15507–15515.
34 L. He, Q. Ni, J. Mu, W. Fan, L. Liu, Z. Wang, L. Li, W. Tang, Y. Liu and Y. Cheng, *J. Am. Chem. Soc.*, 2020, **142**, 6822–6832.
35 Y. Cheng and K. Sun, *J. Fluoresc.*, 2018, **28**, 285–291.
36 M. Derouiche, R. Salhi and S. Baklouti, *Materials*, 2022, **15**, 7828.
37 A. Jaafar, C. Hecker, P. Árki and Y. Joseph, *Bioengineering*, 2020, **7**, 127.
38 R. Thapa, S. Gurung, M.-O. Parat, H. S. Parekh and P. Pandey, *Gels*, 2022, **8**, 99.
39 G. Wang, J. Qin, Y. Feng, B. Feng, S. Yang, Z. Wang, Y. Zhao and J. Wei, *ACS Appl. Mater. Interfaces*, 2020, **12**, 45155–45164.
40 X. Yin, W. Xu, G. Zhu, Y. Ji, Q. Xiao, X. Dong, M. He, B. Cao, N. Zhou, X. Luo, L. Guo and B. Dong, *Nat. Commun.*, 2022, **13**, 6549.
41 B. Sun, R. Ma, X. Wang, S. Ma, W. Li, T. Liu, W. Zhu, Z. Ji, K. S. Hettie and C. Liu, *View*, 2024, **5**, 20230097.
42 L. Liu, S. Wang, B. Zhao, P. Pei, Y. Fan, X. Li and F. Zhang, *Angew. Chem., Int. Ed.*, 2018, **57**, 7518–7522.
43 T. Peng, R. Pu, B. Wang, Z. Zhu, K. Liu, F. Wang, W. Wei, H. Liu and Q. Zhan, *Biosensors*, 2021, **11**, 148.
44 L. Luo, D. Yang and Y. Yang, *Brain-X*, 2023, **1**, e3.
45 E. S. Levy, C. A. Tajon, T. S. Bischof, J. Iafrati, A. Fernandez-Bravo, D. J. Garfield, M. Chamanzar, M. M. Maharbiz, V. S. Sohal, P. J. Schuck, B. E. Cohen and E. M. Chan, *ACS Nano*, 2016, **10**, 8423–8433.
46 H. Zhou, X. Zeng, A. Li, W. Zhou, L. Tang, W. Hu, Q. Fan, X. Meng, H. Deng and L. Duan, *Nat. Commun.*, 2020, **11**, 6183.
47 Y. Chen, J. Chen and B. Chang, *Iradiology*, 2023, **1**, 36–60.
48 H. Wang, W. Ouyang and H. Liu, *Nano TransMed*, 2024, 100032.
49 R. Lv, Y. Wang, B. Lin, X. Peng, J. Liu, W.-D. Lü and J. Tian, *Anal. Chem.*, 2021, **93**, 4984–4992.
50 B. Lin, J. Wu, Y. Wang, S. Sun, Y. Yuan, X. Tao and R. Lv, *Biomater. Sci.*, 2021, **9**, 1000–1007.
51 K. Du, S. Zhao, J. Feng, X. Gao, K. Liu, X. Wang, M. Zhang, Y. Li, Y. Lu and H. Zhang, *J. Mater. Chem. B*, 2021, **9**, 7216–7228.
52 Z. Wang, X. Fu, C. Dai, B. Yang, W. Wang, C. Fan, P. Zhang, J. Sun and D. Sun, *Chem. Eng. J.*, 2024, **480**, 148271.
53 Q. Wang, H. Yang, Y. Liu, Z. Zhou, X. Zhang, M. Sang, F. Xu, L. Song, T. Xia, Y. Zhang, J. Wei, X. Zhang and Q. Ding, *Adv. Healthc. Mater.*, 2023, **12**, e2300420.
54 X. Li, L. Chen, M. Huang, S. Zeng, J. Zheng, S. Peng, Y. Wang, H. Cheng and S. Li, *Asian J. Pharm. Sci.*, 2023, **18**, 100775.
55 W. Li, H. Xin, Y. Zhang, C. Feng, Q. Li, D. Kong, Z. Sun, Z. Xu, J. Xiao, G. Tian, G. Zhang and L. Liu, *Small*, 2022, **18**, e2205647.
56 Y. Wang, M. Feng, B. Lin, X. Peng, Z. Wang and R. Lv, *Nanoscale*, 2021, **13**, 18125–18133.
57 L. Cai, Z. Wang, B. Lin, K. Liu, Y. Wang, Y. Yuan, X. Tao and R. Lv, *Nanoscale Adv.*, 2022, **4**, 2224–2232.
58 T. Grzyb, D. Przybylska, A. Szczeszak, E. Śmiechowicz, P. Kulpiński and I. R. Martín, *Carbohydr. Polym.*, 2022, **294**, 119782.
59 X. Liu, T. Liu, L. Tu, J. Zuo, J. Li, Y. Feng and C. J. Yao, *Small*, 2024, 2308748.
60 M. Liu, Y. Sun, D. B. L. Teh, Y. Zhang, D. Cao and Q. Mei, *Interdiscip. Med.*, 2024, **2**, e20230059.
61 M. Xu, B. Xue, Y. Wang, D. Wang, D. Gao, S. Yang, Q. Zhao, C. Zhou, S. Ruan and Z. Yuan, *Small*, 2021, **17**, 2101397.

 